CrossMark

Precipitation-Induced Grain Growth Simulation of Friction-Stir-Welded AA6082-T6

Q. Wu and Z. Zhang

Friction stir welding of AA6082-T6 with different welding parameters is simulated by computational fluid dynamics model. Monte Carlo method is further used to simulate the grain growth with consideration of the precipitation effects. The comparison with experimental observations can validate the proposed grain growth model with the precipitate effects. Results indicate that the final grain size can be increased by 39.7% in the nugget zone when the volume fraction of precipitation is decreased from 0.8 to 0.2% after welding. Both the grain growth speed and the final grain size on the top surface are higher than the bottom surface. The increase in the welding temperature caused by the increase in the rotation speeds or the axial forces can lead to lower volume fractions of precipitations and then lead to larger grain sizes.

1. Introduction

As a solid-state welding technique invented by TWI in 1991, friction stir welding (FSW) has many advantages in comparison with the conventional fusion welding techniques such as low temperature, low distortion and no pollution (Ref 1). FSW can be applied to join aluminum, magnesium, titanium alloys and even steels (Ref 2, 3) and has been quickly applied to a wide range of industries (Ref 4).

The grain growth is very important for the determination of the friction stir weld quality. So, researches have been focused on the grain structures in friction stir welding. Many experimental works have clarified the relations between final grain structures and service performances of welds. Rajakumar et al. (Ref 5) established an empirical relationship between the post-weld grain sizes and tensile strength in friction-stir-welded aluminum alloy. Safarkhanian et al. (Ref 6) investigated the effect of abnormal grain growth on tensile strength of friction-stir-welded aluminum alloys. Sakthivel and Mukhopadhyay (Ref 7) and Cavaliere and Marco (Ref 8) investigated the microstructure and mechanical properties of friction-stir-welded copper and magnesium alloys, respectively. Different welding parameters and tool geometries are also widely investigated for the optimization of final grain structures. Attallah et al. (Ref 9) studied the factors which can influence the microhardness during FSW of AA5251. Attallah and Salem (Ref 10) reported the controlling of abnormal grain growth during FSW. The effects of tool profiles and weld parameters on the microstructure and mechanical properties are investigated by Xu et al.

(Ref 11). The geometrical recrystallization and the continuous dynamical recrystallization are proved to be the key processes during the grain evolutions. Prangnell and Heason (Ref 12) and Fonda et al. (Ref 13) observed the grain structure evolutions near the welding tools by using 'stop action technique.'

Besides experimental research works, numerical models can provide powerful and efficient way in the research of friction stir welding process (Ref 14). Atharifar et al. (Ref 15) established a CFD model of friction-stir-welded AA6061 to investigate the tool loads and material flows. A CFD model is proposed by Carlone and Palazzo (Ref 16) to analyze the microstructural aspects in AA2024 friction stir welding. Numerical modeling of 3D plastic flow and heat transfer of stainless steels are reported by Nandan et al. (Ref 17). Zhang and Zhang et al. (Ref 18-20, 22) established 3D coupled thermo-mechanical models of FSW to study the material flows and temperature fields. Arora et al. (Ref 21) calculated strains and strain rates during FSW based on a CFD model. Zhang and Zhang (Ref 23) proposed a solid mechanics-based Eulerian model of FSW and focused on the power and heat generations. Several interesting models were proposed to predict the grain structure evolutions. Pan et al. (Ref 24) presented a new smoothed particle hydrodynamics (SPH) model of FSW and predicted microstructure evolutions of magnesium alloys. Saluja et al. (Ref 25) developed a cellular automata coupled finite element (CAFE) model to predict the grain size distribution during friction stir welding and the influence of weld defects on the formation of FSW sheets. Song et al. (Ref 26, 27) used cellular automation modeling in the prediction of recrystallization microstructure evolutions and phase transformations during friction stir welding of titanium alloys. Similar to the cellular automata method, Monte Carlo method is also widely applied in the grain growth simulation in thermo-mechanically coupled process (Ref 28, 29).

Grain growth process in welding zones during FSW is a vital aspect to the joint properties. In previous works (Ref 30, 31), the authors have proposed a Monte Carlo model to simulate the grain growth in friction stir welding of aluminum alloys. In the models, temperature-driven grain growth and strain rate that affected dynamical recrystallization were implemented. However, aluminum alloys usually contain

Q. Wu and Z. Zhang, State Key Laboratory of Structural Analysis for Industrial Equipment, Department of Engineering Mechanics, Faculty of Vehicle Engineering and Mechanics, Dalian University of Technology, Dalian 116024, China. Contact e-mail: zhangz@dlut.edu.cn.

precipitations. Grain growth kinetics and grain boundary migration can be influenced by the precipitations. Many research results have proved that the existence of precipitations can influence the grain growth kinetics of alloys. Nishizawa et al. (Ref 32) examined the Zener relationship between grain size and particle dispersion. Haghighat and Taheri (Ref 33) and Moelans et al. (Ref 34) modeled the grain evolutions by using Monte Carlo method and phase field method, respectively. The influence can be connected to the volume fractions of precipitations, the average sizes of precipitations, the initial grain sizes (Ref 35), and the dispersion and morphology of precipitations (Ref 36). However, the detailed influences and mechanisms about grain growth with the pinning effect in friction-stir-welded aluminum alloys are seldom reported. So based on previous works (Ref 30, 31), we present a computational fluid dynamics model of AA6082-T6 coupled with a Monte Carlo simulation method to predict the grain growth process with the considerations of pinning effect caused by precipitations. Five different welding conditions are simulated to investigate the influence of different welding parameters on the width distributions of the stirring zones. Several positions in the stirring zones in each case are selected to study the detailed thermal and mechanical experience of welded materials. Then, the grain growth kinetics with the consideration of precipitations is simulated.

2. Model Description

2.1 CFD Model of FSW

A computational fluid dynamics (CFD) model is used to simulate the friction stir welding process. The material of welded plates in this work is chosen to be AA6082-T6, and it is modeled by a visco-plastic flow field in CFD model. The thermal and flow problems were coupled together during the solving process. The constitutive law of the modeled material is defined by:

$$\dot{\bar{\varepsilon}} = A_0 [\sin h(\alpha_0 \bar{\sigma})]^{n_0} e^{(-Q/RT_{abs})} \tag{Eq 1}$$

where T_{abs} is the absolute temperature. Q is activity energy and equals 146 kJ mol^{-1}(Ref 37). R is gas constant and equals 8.31 J mol^{-1} K^{-1}. α_0, n_0 and A_0 are equation coefficients, which are derived from experimental tests (Ref 37), and the values are taken as 6.49, 0.0238 and 8.0×10^9, respectively. $\dot{\bar{\varepsilon}}$ is the equivalent strain rate, and $\bar{\sigma}$ is the flow stress.

When CFD model is used to simulate the visco-plastic flow of the heated metals, the viscosity of the fluid fields should be calculated from the flow stress and equivalent strain rate (Ref 38):

$$\mu = \frac{\bar{\sigma}}{3\dot{\bar{\varepsilon}}} \tag{Eq 2}$$

Average equivalent strain rate magnitude in stirring zones is used to simplify the iterations in Eq 1 and 2; the strain rate tensor components are calculated from the velocity gradient (Ref 21):

$$\dot{\varepsilon}_{ij} = \frac{1}{2} \left(\frac{\partial u_i}{\partial x_j} + \frac{\partial u_j}{\partial x_i} \right) \tag{Eq 3}$$

Then the equivalent strain rate magnitude is calculated by:

$$\dot{\bar{\varepsilon}} = \sqrt{\frac{2}{3} \dot{\varepsilon}_{ij} \dot{\varepsilon}_{ij}} \tag{Eq 4}$$

The thermal properties such as heat conductivity and specific heat of AA6082-T6 are considered to be functions of temperatures during the computing, and the detailed values used in this work can be found in Table 1 according to a previously established CFD model of FSW in Ref 39.

Figure 1 illustrates the schematic of CFD model. The welding tool is fixed at the middle position of the plate. The motions of welding tool are represented by the boundary conditions. The transverse speed is represented by the inlet velocity. Velocity of materials at the shoulder and pin contact surfaces is defined to be the same with the rotation speed of the welding tool (Ref 38).

During FSW process, the heat can be generated from both the friction and the plastic deformation. But the plastic dissipation cannot be directly incorporated in CFD model. This is the reason that the heat input on the contact surfaces used in CFD model is generally larger than the solid mechanics-based model (Ref 19, 23). The current method for prediction of temperature field has been validated in previous works (Ref 39, 40).

On the shoulder contact surface, the heat input power is computed by (Ref 40):

$$P_s = \frac{4}{3} \pi^2 \mu_f \frac{F_p}{A_s} \frac{\omega_0}{60} \left(r_s^3 - r_p^3 \right) \tag{Eq 5}$$

where μ_f is the friction coefficient, which varies with the rotation speed. F_p is the axial force acted on the shoulder contact surface. A_s is the area of shoulder contact surface. ω_0 is the rotation speed of the shoulder. r_s and r_p are the radii of shoulder and welding pin, respectively.
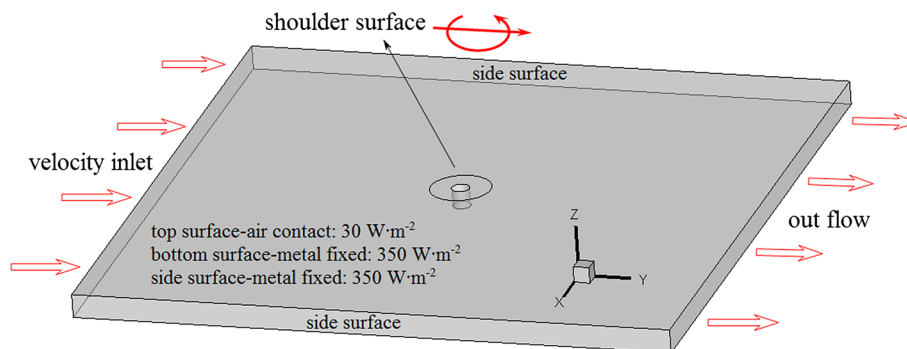

Fig. 1 CFD model of FSW

Table 1 Temperature-dependent properties of material modeled

Temperature, K	Specific heat, $J\ Kg^{-1}\ K^{-1}$	Conductivity, $W\ m^{-1}\ K^{-1}$	Poisson's ratio
273	917	162	0.23
366	978	177	
477	1024	192	
588	1078	207	
700	1133	223	

Table 2 Boundary conditions and thermal properties (Ref 39, 41)

Part	Modeled condition	Thermal values
Top surface of plate	Contacting air	$30\ W\ m^{-2}$
Two side surface	Contacting metal fixture	$350\ W\ m^{-2}$
Bottom surface	Contacting metal fixture	$350\ W\ m^{-2}$
Inlet materials	Room temperature	300 K
Modeled materials	Heat transfer	Temperature dependent

Heat input power on the side surface of the welding pin is calculated from the pressure acted on the pin (Ref 40):

$$P_{ps} = \int_0^{2\pi} \int_0^h 2\pi \mu_f p_{ps} \frac{\omega_0}{60} r_p^2 \mathrm{d}z \mathrm{d}\theta \tag{Eq 6}$$

where p_{ps} is the pressure acted on the side surface of welding pin, which is derived from the flow field. h is the length of the pin.

The bottom and the two side surfaces of the plates are assumed to keep contact with metal fixtures. The thermal boundary conditions of these surfaces are set as heat convection of $350\ W\ m^{-2}$ according to Ref 41. Top surface is exposed to the air and the heat convection is set as $30\ W\ m^{-2}$ (Ref 41). The heat transfer boundary conditions and the heat convective coefficient of the modeled materials are summarized in Tables 1 and 2.

The models are established and calculated by ANSYS FLUENT solver based on finite volume method. ANSYS FLUENT uses a control-volume-based technique to convert a general scalar transport equation to an algebraic equation that can be solved numerically. The following equation in discrete form is applied to each meshed cell in the computational domain during the solving:

$$\frac{\partial \rho \phi}{\partial t} V + \sum_f^{N_f} \rho_f \vec{v}_f \phi_f \cdot \vec{A}_f = \sum_f^{N_f} {}_\phi \nabla \phi_f \cdot \vec{A}_f + S_\phi V \tag{Eq 7}$$

where ρ is the density, ϕ is transported scalar quantity, V is the control cell volume, N_f is the number of faces enclosing meshed cell, ϕ_f is the value of ϕ convected through face f, $\rho_f \vec{v}_f \phi_f \cdot \vec{A}_f$ is the mass flux through the face, and S_ϕ is the source of ϕ per unit volume.

The computing zone has been meshed into 837771 tetrahedral cells and 173369 nodes to guarantee computing precision. Material properties, which are depending on the temperature fields, viscosity of the flow and boundary conditions, are defined by compiled C language during the iterations. It is obviously known that both the increase in axial forces and rotation speeds can increase the temperature fields of welded plates. So a series of cases with different welding parameters are simulated to study the detailed influence of axial forces and

rotation speeds on the FSW process and final microstructures in the stirring zones. The dimensions and the welding parameters used in this work are shown in Table 3. In cases 1-3, the welding speeds keep constant, but the axial forces are increased from 2.2 to 2.8 kN. In cases 4, 2 and 5, the axial forces are kept as 2.5 kN, but the rotation speeds are increased from 500 to 1000 r min^{-1}. Axial forces are selected according to experiments on FSW of 6xxx series aluminum alloys (Ref 42, 43).

In order to validate the model, one case with the same welding parameters and dimensions of welding plate with the experimental conditions from Ref 42 is calculated. The predicted temperature values across the welding seam are compared and validated with the measured values, as shown in Fig. 2.

2.2 Microstructure Simulation Model

In this work, a Monte Carlo algorithm is used to simulate grain structure evolutions in stirring zones of modeled cases. A real square area of S_a mm^2 in stirring zone is represented by a $N \times N$ lattices system. Each lattice point has been given a number among $1 \sim q$ to describe its crystallographic orientations. If adjacent lattices have the same number of orientation, then they are considered to form one grain as shown in Fig. 3. At the initial step of simulation, randomly picked orientations are given to each lattice site. At each grid point, the energy of lattice is calculated from the Hamiltonian (Ref 44):

$$E = -J \sum_{i=1}^m (\delta_{q_i q_j} - 1) \tag{Eq 8}$$

where J is a positive constant representing the grain boundary energy. m is the total number of sites near one lattice point, which is equal to 8 in current model. δ is the Kronecker function. The total energy of the lattice system can be derived by the summation of all grid points.

During the whole welding periods, grains in the welding zones can grow due to the grain boundary migration. The driving force of this process is the reduction in grain boundary areas and reduction in grain boundary energies. In Monte Carlo simulation, reorientation is used to model this process. During each reorientation step, a lattice site at random position can be chosen and its orientation is trying to change to a new randomly picked one. The possibility of acceptance of the new orientation p can be calculated by the change of lattice system's total energy (Ref 44):

$$p = \begin{cases} 1, & \Delta E \leq 0 \\ e^{-\frac{\Delta E}{k_B T_{abs}}}, & \Delta E > 0 \end{cases} \tag{Eq 9}$$

where ΔE is the system's energy change during reorientation. k_B is the Boltzmann constant. During the computation of

Table 3 Dimensions and welding parameters

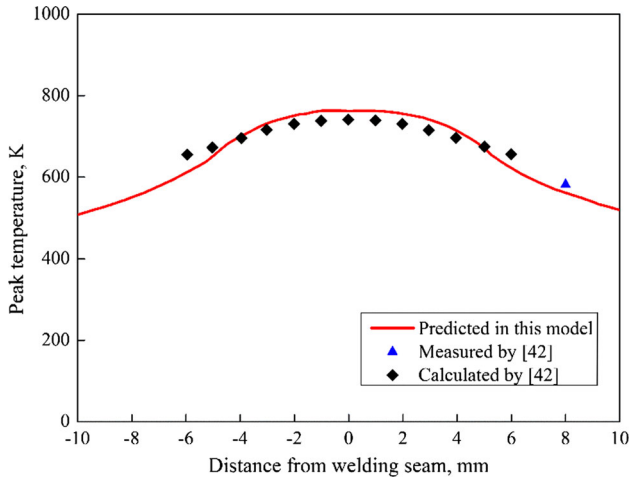|	Dimensions, mm	Rotation speed, r min^{-1}	Transverse speed, mm min^{-1}	Axial force, kN	Shoulder and pin diameters, mm
Case 1	$100 \times 100 \times 3$	715	71.5	2.2	10 and 3
Case 2	$100 \times 100 \times 3$	715	71.5	2.5	10 and 3
Case 3	$100 \times 100 \times 3$	715	71.5	2.8	10 and 3
Case 4	$100 \times 100 \times 3$	500	71.5	2.5	10 and 3
Case 5	$100 \times 100 \times 3$	1000	71.5	2.5	10 and 3
Temperature validation (Ref 42)	$100 \times 100 \times 3$	1040	100	2.6	10 and 3

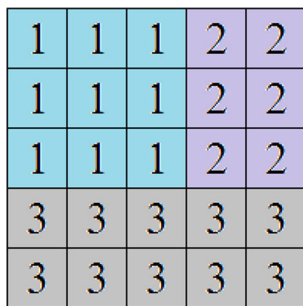**Fig. 2** Validation of FSW model with 1040 r min^{-1} and 100 mm min^{-1}

Fig. 3 Schematic of lattice system

acceptance possibility in Eq 9, the value of term $\frac{J}{k_B T_{abs}}$ is assumed to be 1 (Ref 45). In each MC step, the above reorientation iteration is repeated for N^2 times.

Materials in stirring zone suffer severe deformation and high temperature. In the cooling periods, the recrystallization phenomenon must be considered in the model along with Monte Carlo simulation of grain growth. In this model, the recrystallized nucleus is created on the boundaries of grains. The acceptance of created recrystallization nucleus is subjected to a probability, which is calculated from the rate of nucleation proposed by Ding and Guo (Ref 46):

$$P_{nucl} = D\dot{\bar{\varepsilon}}_{max} \exp\left(-\frac{Q}{RT_{abs}}\right) \qquad \text{(Eq 10)}$$

where D is a ratio constant and is chosen as 10^3. $\dot{\bar{\varepsilon}}_{max}$ is the maximum value of equivalent strain rate magnitude experi-

Table 4 Maximum temperature vs. volume fraction of precipitations in the model (Ref 47, 48)

Temperature, K	Volume fraction, %
300	1.60
400	1.20
500	0.98
600	0.87
700	0.55
773	0

enced by materials along the streamlines. The nucleation rate for recrystallization is considered as the functions of both temperature and deformation in the stirring zone. During each Monte Carlo step, lattice sites located at grain boundaries can be chosen for one time and can be decided whether to be changed to a nucleation embryo according to the above probability.

In order to incorporate precipitations into the model to study the pinning effect on grain boundary movement, a special orientation $q_i = q + 1$ is assigned to lattice sites that represent the precipitations. One lattice site is chosen to represent one particle of precipitation in this model. The number of inserted precipitations is computed according to the volume fraction (V_f) of precipitations. In the experimental and numerical works reported by Bardel et al. (Ref 47) and Myhr et al. (Ref 48) of 6xxx series aluminum alloys, it is proved that the volume fraction of precipitations decreases with the increase in temperature. The reported relationship is a nonlinear function. In this work, V_f is assumed to be constant during each individual Monte Carlo simulation case. The value of V_f is chosen from Table 4, according to Ref 47, 48. The maximum temperature experienced by materials of each thermal cycle is used for the determination of V_f.

The Monte Carlo simulation procedure is controlled by the MC steps. It is important to build the relationship between the MC steps and the real time during the welding. CFD model provides the histories of thermal cycles versus real time, and then, MC steps are calculated from the thermal cycles by several empirical and analytical functions. The simulated average grain size could be fitted as a function:

$$L = K_1 \lambda (MCS)^{n_1} \qquad \text{(Eq 11)}$$

where L is the simulated average grain size, and it is estimated from the total number of grains n_0 in the system by: $L = \sqrt{S_a/n_0}$.

The grow rate of grains and the velocity of grain boundary migration v are assumed to follow a relation (Ref 30, 31):

Table 5　The parameters used in the model

Parameter	Value	Reference
Average number per unit area, Z	4.31×10^{20} atoms m^{-2}	…
Planck's constant, h	6.624×10^{-34} J s	…
Accommodation probability, A	1.0	Ref 30
Avagadro's number, N_a	6.02×10^{23} mol^{-1}	…
Atom molar volume, V_m	1.0×10^{-5} m^3 mol^{-1}	…
Fusion entropy, ΔS_f	11.5 J mol^{-1} K^{-1}	Ref 50
Boundary energy, γ	0.5 J m^{-2}	Ref 51
Ratio constant, α	1.0	Chosen
Ratio constant, n	0.4, $T_{max} > 550$ K	Chosen
	0.5, $T_{max} > 700$ K	
Activation enthalpy, Q	146 kJ mol^{-1}	Ref 37

$$\frac{dL}{dt} = \alpha v^n \qquad (\text{Eq } 12)$$

where α and n are material parameters.

And v is defined as (Ref 49):

$$v = \frac{AZV_m^2}{N_a^2 h} \exp\left(\frac{\Delta S_f}{R}\right) \exp\left(-\frac{Q}{RT}\right)\left(\frac{2\gamma}{L}\right) \qquad (\text{Eq } 13)$$

In Eq 13, A, Z, V_m, R, N_a and h are physical constants. ΔS_f and γ are material parameters of aluminum alloys. The values of parameters in this model are summarized in Table 5 (Ref 30, 37, 50, 51). Then, the relation of MC steps versus time t can be obtained by combination of Eq 11 and 13,

$$(MCS)^{(n+1)n_1} = \left(\frac{L_0}{K_1\lambda}\right)^{n+1} + \frac{(n+1)\alpha C_1^n}{(K_1\lambda)^{n+1}} \sum \left[\exp^n\left(-\frac{Q}{RT_i}\right)t_i\right] \qquad (\text{Eq } 14)$$

where $C_1 = \frac{2A\gamma ZV_m^2}{N_a^2 h}\exp\left(\frac{\Delta S_a}{R}\right)$ is the integration constant.

In order to validate the microstructure simulations in the proposed recrystallization model, an example in comparison with the experimental observation in friction stir welding of pure aluminum reported by Morisada et al. (Ref 52) is selected. All the parameters used in the validation model are exactly the same with the Ref 52. Monte Carlo steps are calculated from the thermal cycle estimated by the velocity time history and the measured maximum temperature (713 K) (Ref 52). Different strain rates are used to validate the recrystallization model. Three grain growth cases at strain rates of 9, 11 and 13.4 s^{-1} are examined. The validated results are illustrated in Fig. 4. The predicted grain sizes and grain microstructures match well with the observed results (Ref 52).

3. Results and Discussion

3.1 Temperature Distribution and Materials Flow

The peak temperatures of the simulated five cases are illustrated in Fig. 5. Temperature contour on the top surface in case 2 is showed as an example due to the similar contour shapes in different cases. The temperature fields are symmetrical along the welding seam. The maximum temperature appears at the shoulder contact surface. Temperatures decrease rapidly with the increase in distance from the welding tool. Temperature gradient is not the same before and behind the
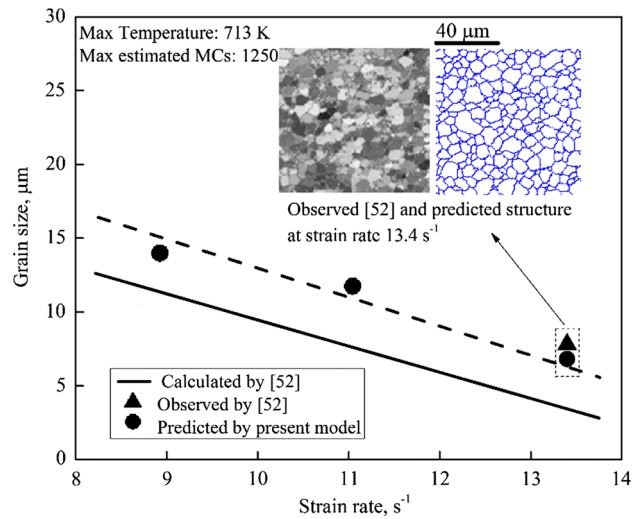

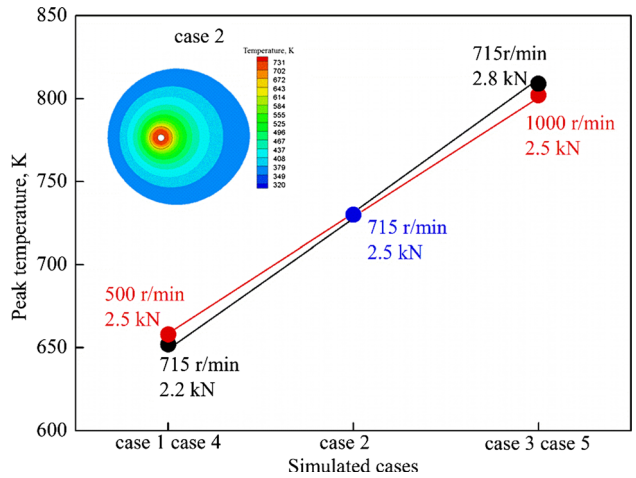**Fig. 4** Validation of the recrystallization model influenced by different strain rates

Fig. 5 Temperature field and peak temperature of simulated cases

welding tool, so the shapes of temperature contours are similar to ellipses. Both the increase in axial pressure and rotation speed can increase the welding temperature. Peak temperature increases from 658 to 802 K when the rotation speed increases from 500 to 1000 r min^{-1} in cases 4, 2 and 5. When the axial force increases from 2.2 to 2.8 kN in cases 1, 2 and 3, peak temperature increases from 652 to 809 K.

Based on the calculated velocity fields, streamlines of the simulated materials flow can be derived. Figure 6 shows the streamlines of materials flow on top and bottom surfaces in case 4 as an example. The directions of rotation and transverse speeds are the same with the directions in Fig. 1. The materials' flow paths indicate that the severe materials flow mainly occurs at the shoulder contact surface. Materials at the advancing side flow around the pin to the retreating side and finally deposit behind the welding tool. The simulated materials flow and streamlines agree well with the experimental and numerical results reported in Ref 53. Compared with experimental works, numerical simulations are more convenient to study the ranges of stirring zones according to numerical predicted streamlines. In stirring zone, materials suffer severe deformations and rotate around the tool pin to form the nugget zones. The profile of

streamlines in stirring zones was illustrated as high-density and closed velocity vector circles (Ref 54). By this criterion, the range of stirring zones of different cases could be specified from the path lines. In Fig. 6, dashed lines have marked the ranges of stirring zones. The widths of stirring zones on top and bottom surfaces of simulated cases are summarized in Table 6, where the minus values represent the width from retreating sides and the positive values represent the width from advancing sides. The welding seam is located at 0 mm.

Obviously, materials on bottom surfaces are not directly stirred by welding tools. The width of stirring zone on bottom surfaces is smaller than that on top surfaces. The ranges of stirring zones at the advancing sides are wider than the retreating sides, which is caused by the different flow characteristics at the two sides. It is notable that the range of stirring zones is also increased on both top and bottom surfaces when the rotation speeds and axial forces are increased.

Thermal cycles and deformation histories extracted along the streamlines are the basic data to investigate the microstructure evolutions in stirring zones. From the contours of temperature distribution in Fig. 5, it is clearly seen that the temperature decreases with the increase in distance from the welding seam. Then, in order to investigate the regulations between temperature histories and path lines' positions, temperature versus time, which is extracted from path lines at different sides and surfaces in stirring zones, is exhibited in Fig. 7. The tendency of all the temperature history curves is similar. The temperature quickly rises when the path line approaches the stirring zone and quickly drops when the path line leaves the stirring zone. Peak temperatures along path lines at advancing sides and retreating sides are similar. Peak temperatures on top surfaces are higher than that on bottom surfaces. Thermal cycles along streamlines at various positions could be extracted to calculate MC simulation steps by Eq 14.
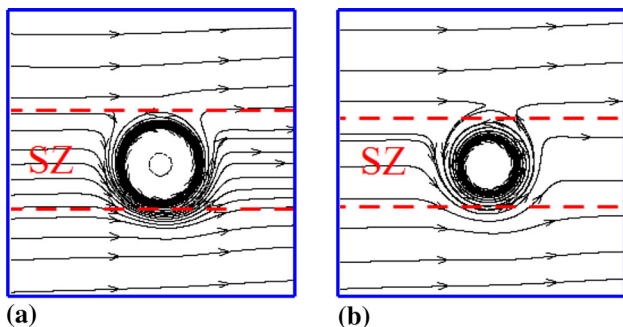
Maximum equivalent strain rates along different streamlines are illustrated in Fig. 8. The equivalent strain rates reach peak values when the materials flow into the stirring zones. Equivalent strain rates at the advancing sides are higher than that at the retreating sides. At the advancing side, the maximum $\dot{\bar{\varepsilon}}$ increases with the increase in distance to the welding seam within the stirring zone. At the retreating side, the maximum $\dot{\bar{\varepsilon}}$ decreases with the increase in distance to the welding seam within the stirring zone. This is caused by the different features of path lines at advancing and retreating sides. $\dot{\bar{\varepsilon}}$ near the bottom surface is much smaller than top surface due to the lower material flow. The increase in the axial forces and the rotation speeds can lead to the increase in temperature and the flowability of materials. As a consequence, $\dot{\bar{\varepsilon}}$ is increased with the increase in the axial forces and the rotation speeds. Peak value of $\dot{\bar{\varepsilon}}$ in the five cases reaches 74.1 s^{-1} on the top surface in case 5, while the minimum value of $\dot{\bar{\varepsilon}}$ is only 11.8 s^{-1} on bottom surface in case 4. The above equivalent strain rate histories computed based on velocity fields in stirring zones are reasonable compared with reported values in Ref 55, 56. The computed strain rate histories can be used in the recrystallization evolution models for the prediction of the grain growth.

3.2 Microstructure Evolutions

In this model, a grid system which consists of 600×600 lattice sites is used to simulate a real area of 400×400 μm^2 in stirring zones at different positions. The number of orientations q is equal to 100. This means each grid site represents approximately 0.67 μm real length. The lattice number is sufficient in accuracy to model grain boundary immigration that forced grain growth and precipitation evolutions compared with values in Ref 57-59. In order to determine the system constants K_1 and n_1, grain growth process without recrystallization and pinning effect is simulated. From linearly fitted function of the grain growth kinetics relation, the system constants are computed. K_1 equals 1.0 and n_1 equals 0.46, respectively. The value of grain growth time exponent n_1 calculated in this model agrees well with the value reported in Ref 45.

Based on the extracted thermal cycles and deformation histories along flow streamlines at different positions in the selected cases, grain microstructure evolutions with considerations of pinning effect and recrystallization can be simulated. Figure 9 shows the volume fractions of precipitations and MC steps of simulated cases at different positions. From Fig. 9(a), it can be seen that values of V_f increase with the increase in distance to the welding center. Values of V_f are lower on the top surfaces than that on the bottom surfaces. At top surfaces in case 3 and case 5, V_f can decrease to 0 due to the fact that the maximum temperatures exceed 770 K. According to Eq 14, Monte Carlo simulation steps are connected to the thermal
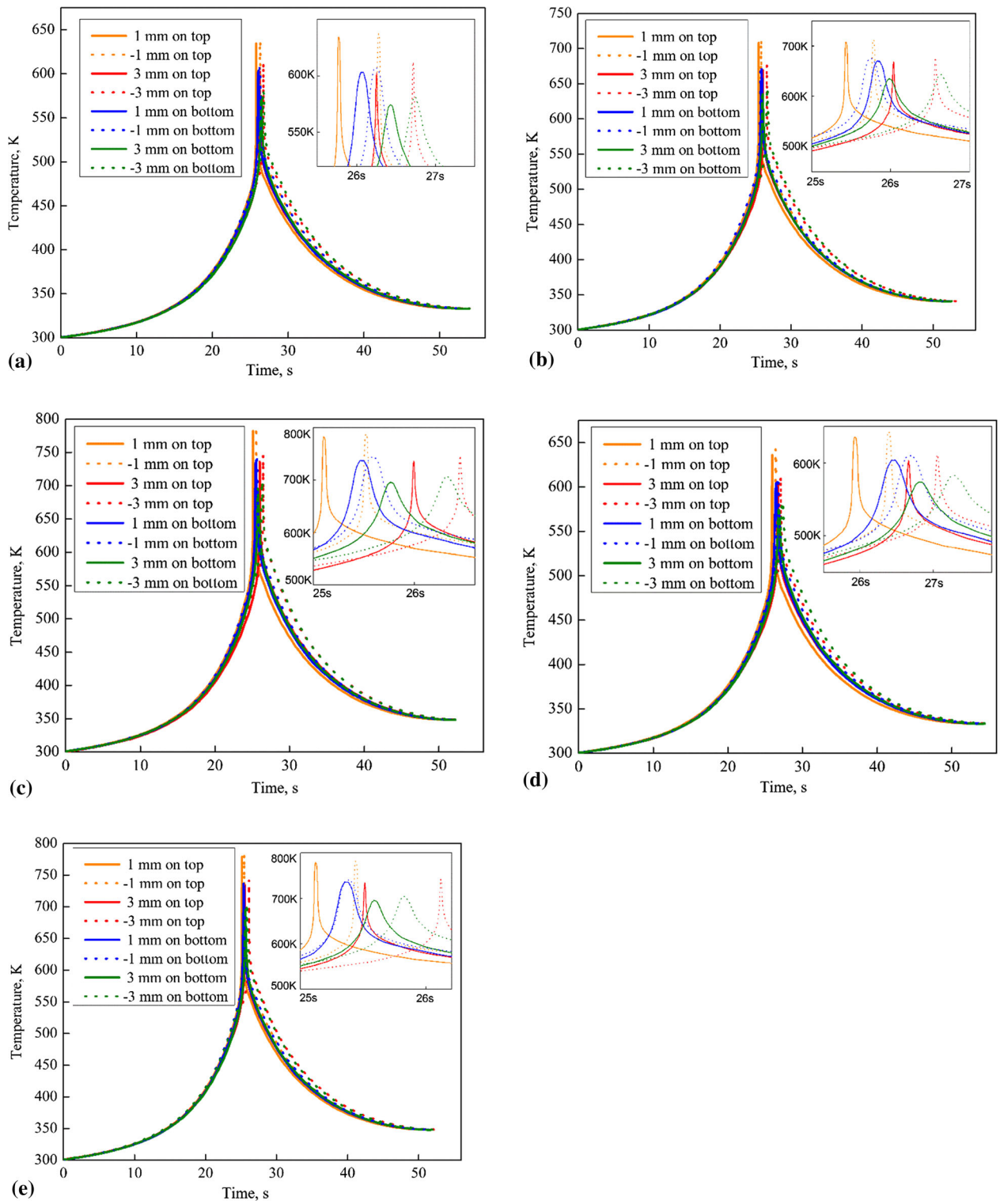

Fig. 6 Flow streamlines on top and bottom surfaces of case 4. (a) Top surface, (b) bottom surface

Table 6 Predicted ranges of stirring zones

mm	Case 1715 r min^{-1} 2.2 kN		Case 2715 r min^{-1} 2.5 kN		Case 3715 r min^{-1} 2.8 kN		Case 4500 r min^{-1} 2.5 kN		Case 51000 r min^{-1} 2.5 kN	
Width of SZ on top surface	12.4	−6.0 6.4	12.5	−6.0 6.5	12.6	−6.1 6.5	12.2	−5.9 6.3	12.8	−6.2 6.6
Width of SZ on bottom surface	9.1	−4.0 5.1	9.1	−4.0 5.1	9.2	−4.1 5.1	8.9	−4.0 4.9	9.4	−4.2 5.2

Fig. 7 Temperature extracted along streamlines in cases. (a) Case 1, (b) case 2, (c) case 3, (d) case 4, (e) case 5

cycle along streamlines. In Fig. 9(b), it can be seen that MC steps decrease with the decrease in peak temperatures.

Interpolated contours of predicted grain sizes in stirring zones are illustrated in Fig. 10. The results show that the final simulated grain sizes are an obviously positive correlation to the temperature distributions. Grain sizes on the top surfaces are higher than that on the bottom surfaces, which is in accordance with experimental observations (Ref 55). The grain size decreases with the increase in the distance from the center welding seam. Average grain sizes increase with the increase in axial forces and rotation speeds. Predicted maximum grain size appears on the top surface in case 3 which can reach 13.96 μm. Grain sizes at advancing sides and retreating sides are almost symmetrical. In case 2, the contour of grain size is more
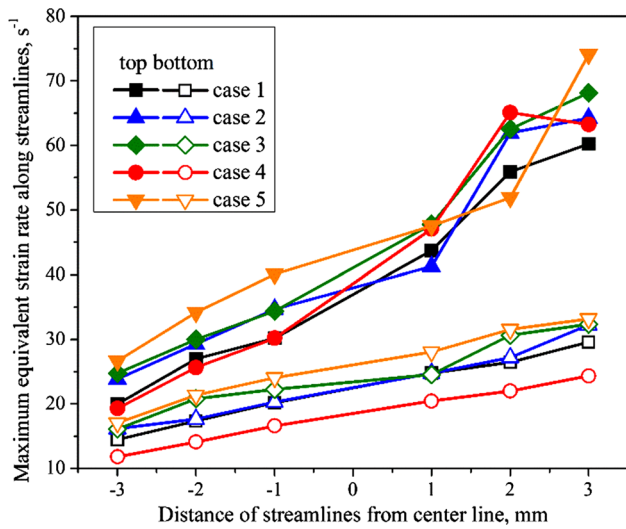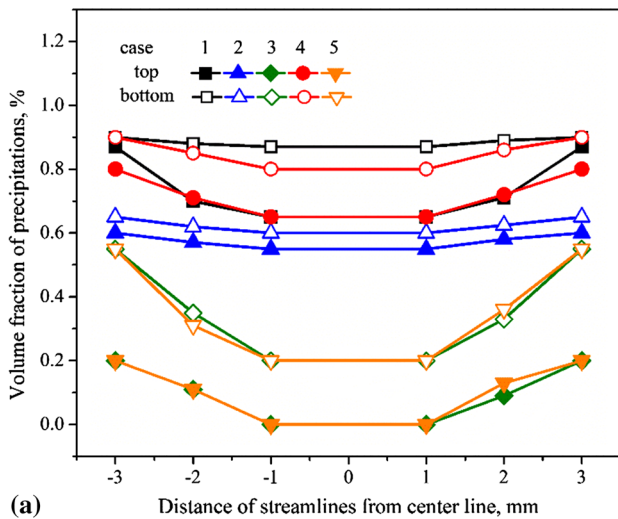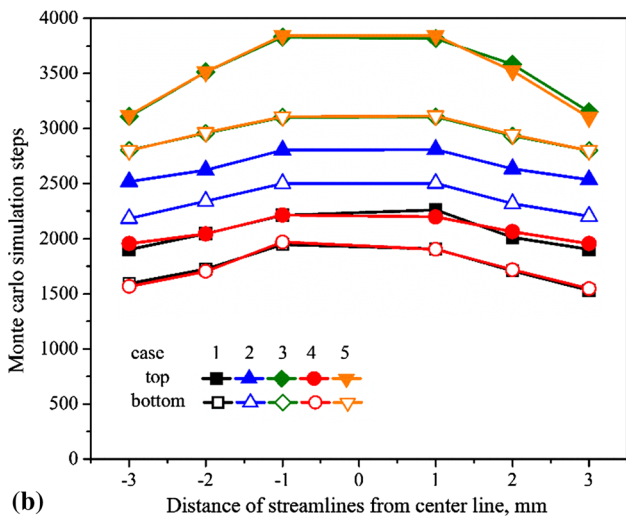
Fig. 8 Maximum equivalent strain rate along streamlines

Fig. 10 Interpolated contours of predicted grain sizes in stirring zones of simulated five cases

(a)

(b)

Fig. 9 Volume fractions of precipitations and Monte Carlo steps at different positions. (a) Volume fraction of precipitations at different positions, (b) Monte Carlo simulation steps at different positions
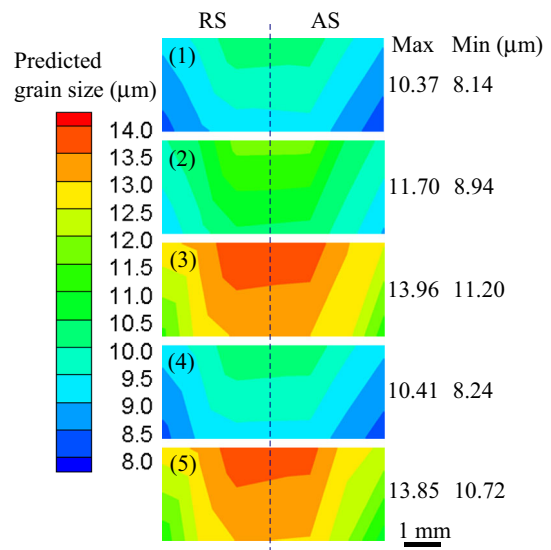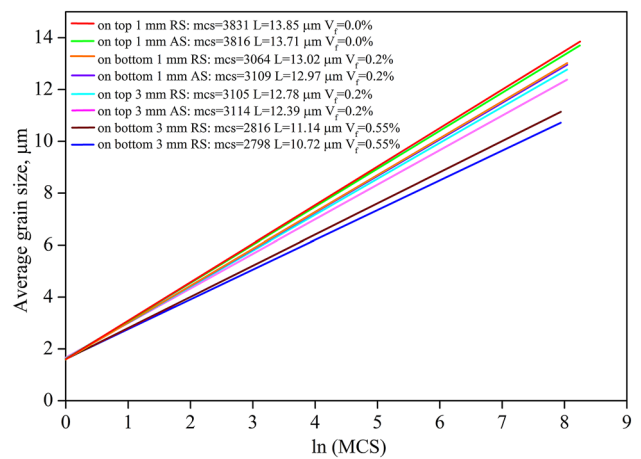

Fig. 11 Simulated grain growth process in case 5

uniform than other cases, which is caused by more uniformly distributed values of V_f and MC steps in stirring zone, as shown in Fig. 10. When the welding parameters used in the simulation are 715 r min^{-1} and 71.5 mm s^{-1} of case 2, the final predicted average grain size in stirring zones is 11.5 μm, and this predicted value agrees well with the experimental observations reported in Ref 60 of average grain size 11.7 μm in stirring zone with the same welding parameters.

In order to exhibit the detailed grain growth in stirring zones, the relations between L and ln(MCS) at several chosen positions in case 5 are described in Fig. 11 as an example. The values of the eight curves' slopes represent the growing speeds during the iterations of simulated grains. It is obviously seen that higher values of V_f can reduce the grain growth rate. The pinning effect becomes more evident with higher V_f. When the iterations of Monte Carlo simulation steps are identical, average grain size becomes bigger in the cases with lower level of pinning effect. The grain growth rate on bottom surfaces is obviously lower than the top surfaces. This phenomenon has proved that higher volume fraction of precipitations can hinder
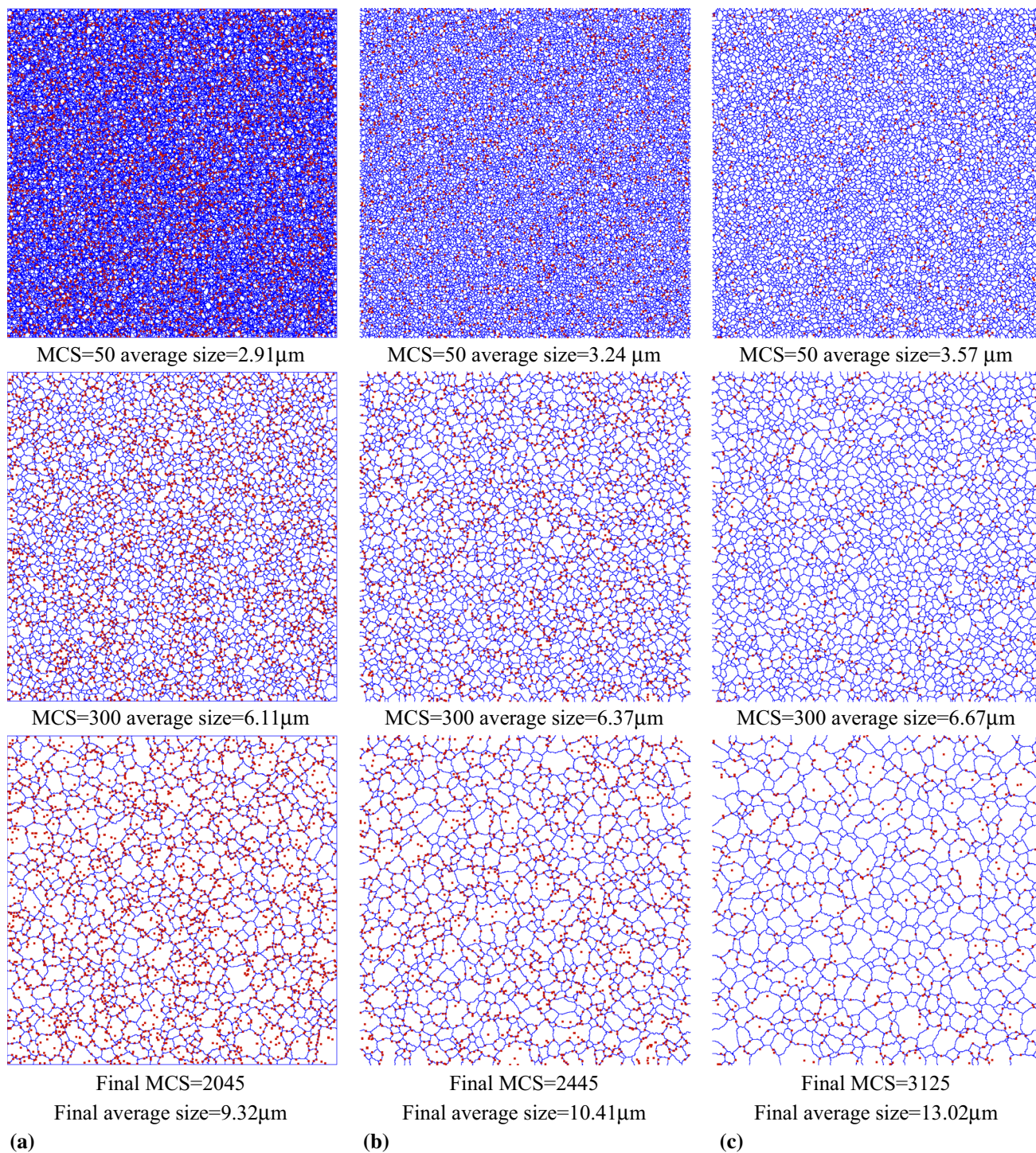
MCS=50 average size=2.91μm   MCS=50 average size=3.24 μm   MCS=50 average size=3.57 μm

MCS=300 average size=6.11μm   MCS=300 average size=6.37μm   MCS=300 average size=6.67μm

Final MCS=2045   Final MCS=2445   Final MCS=3125
Final average size=9.32μm   Final average size=10.41μm   Final average size=13.02μm

(a)   **(b)**   **(c)**

Fig. 12 Simulated microstructure evolutions. (a) On bottom surface, 1 mm at RS, case 1 (V_f = 0.8%). (b) On bottom surface, 1 mm at RS, case 2 (V_f = 0.5%). (c) On bottom surface, 1 mm at RS, case 3 (V_f = 0.2%)

the migration of grain boundaries. It is notable that grain growth rates at advancing sides are slightly lower than that at retreating sides due to the different recrystallization probabilities at the two welding sides. Equivalent strain rates are higher at advancing sides than that at retreating sides. The higher values of $\dot{\bar{\varepsilon}}$ lead to a higher probability for the acceptance of recrystallized crystal nucleus during the calculation.

Figure 12 compares three cases with different levels of precipitations. V_f is 0.8% in Fig. 12(a), 0.5% in Fig. 12(b) and 0.2% in Fig. 12(c), respectively. The grain boundaries are represented by blue lines, and the precipitations are represented by red points in Fig. 12. The positions for the grains shown in Fig. 12 are 1 mm away from the centerline at the retreating sides on the bottom surface. The maximum equivalent strain

rates on the selected positions are similar. So, the recrystallization and the nucleation in the three cases are almost the same. The only different factor that affects the grain growth rates is the pinning effect. The pinning effect of precipitations on the grain boundary movement is obviously seen from the comparison of the microstructures. At the same Monte Carlo steps shown in Fig. 12, larger average grain size can be obtained at lower volume fraction.

4. Conclusions

Grain structure evolutions during friction stir welding of AA6082-T6 are investigated with the presence of precipitations via a Monte Carlo simulation method and CFD model. Five cases with different axial forces and rotation speeds are simulated to study the effect of the process parameters on the thermal cycles, flow patterns, equivalent strain rates, widths of welding zones, the final grain sizes and the grain structures. The main results are summarized as follows:

1. Precipitations can hinder the grain boundary immigrations and then decrease the grain growth rate. With the increase in axial forces and rotation speeds, the volume fractions of precipitations decrease. Lower volume fractions of precipitations can increase grain growth rates and final grain sizes.
2. The volume fraction of precipitations varies with the positions in the stirring zones evidently. The volume fraction increases with the increase in distance to the center line quickly. The volume fraction of precipitation is higher on the bottom surfaces than that on the top surfaces. Grain growth rates are higher at the positions with lower volume fraction of precipitation in the stirring zones.
3. Grain growth rates are slightly higher at the retreating sides than that at the advancing sides. This is caused by the different maximum equivalent plastic strain rates at the advancing and retreating sides. The possibility of acceptance of recrystallized crystal nucleus increases with the increase in the maximum equivalent plastic strain rates.

References

1. Z.Y. Ma, Friction Stir Processing Technology: A Review, *Metall. Mater. Trans. A*, 2008, **39**, p 642–658
2. G. Çam, Friction Stir Welded Structural Materials: Beyond Al-Alloys, *Int. Mater. Rev.*, 2013, **56**, p 1–48
3. G. Çam and S. Mistikoglu, Recent Developments in Friction Stir Welding of Al-Alloys, *J. Mater. Eng. Perform*, 2014, **23**, p 1936–1953
4. B.T. Gibson, D.H. Lammlein, T.J. Prater, W.R. Longhurst, C.D. Cox, M.C. Ballun, K.J. Dharmaraj, G.E. Cook, and A.M. Stauss, Friction Stir Welding: Process, Automation, and Control, *J. Manuf. Process.*, 2014, **16**, p 56–73
5. S. Rajakumar, C. Muralidharan, and V. Balasubramanian, Establishing Empirical Relationships to Predict Grain Size and Tensile Strength of Friction Stir Welded AA 6061-T6 Aluminium Alloy Joints, *Trans. Nonferr. Met. Soc. China*, 2010, **20**, p 1863–1872
6. M.A. Safarkhanian, M. Goodarzi, and S.M.A. Boutorabi, Effect of Abnormal Grain Growth on Tensile Strength of Al-Cu-Mg Alloy Friction Stir Welded Joints, *J. Mater. Sci.*, 2009, **44**, p 5452–5458
7. T. Sakthivel and J. Mukhopadhyay, Microstructure and Mechanical Properties of Friction Stir Welded Copper, *J. Mater. Sci.*, 2007, **42**, p 8126–8129
8. P. Cavaliere and P.P.D. Marco, Effect of Friction Stir Processing on Mechanical and Microstructural Properties of AM60B MAGNESIUM ALLOY, *J. Mater. Sci.*, 2006, **41**, p 3459–3464
9. M.M. Attallah, C.L. Davis, and M. Strangwood, Microstructure-Microhardness Relationships in Friction Stir Welded AA5251, *J. Mater. Sci.*, 2007, **42**, p 7299–7306
10. M.M. Attallah and H.G. Salem, Friction Stir Welding Parameters: A Tool for Controlling Abnormal Grain Growth During Subsequent Heat Treatment, *Mater. Sci. Eng. A*, 2005, **391**, p 51–59
11. W.F. Xu, J.H. Liu, H.Q. Zhu, and L. Fu, Influence of Welding Parameters and Tool Pin Profile on Microstructure and Mechanical Properties Along the Thickness in a Friction Stir Welded Aluminum Alloy, *Mater. Des.*, 2013, **47**, p 599–606
12. P.B. Prangnell and C.P. Heason, Grain Structure Formation During Friction Stir Welding Observed by the 'Stop Action Technique', *Acta Mater.*, 2005, **53**, p 3179–3192
13. R.W. Fonda, J.F. Bingert, and K.J. Colligan, Development of Grain Structure During Friction Stir Welding, *Scr. Mater.*, 2004, **51**, p 243–248
14. D.M. Neto and P. Neto, Numerical Modeling of Friction Stir Welding Process: A Literature Review, *Int. J. Adv. Manuf. Technol.*, 2013, **65**, p 115–126
15. H. Atharifar, D. Lin, and R. Kovacevic, Numerical and Experimental Investigations on the Loads Carried by the Tool During Friction Stir Welding, *J. Mater. Eng. Perform.*, 2009, **18**(4), p 339–350
16. P. Carlone and G.S. Palazzo, A Numerical and Experimental Analysis of Microstructural Aspects in AA2024-T3 Friction Stir Welding, *Key Eng. Mater.*, 2013, **554**, p 1022–1030
17. R. Nandan, G.G. Roy, T.J. Lienert, and T. DebRoy, Numerical Modelling of 3D Plastic Flow and Heat Transfer During Friction Stir Welding of Stainless Steel, *Sci. Technol. Weld. Join.*, 2006, **11**, p 526–537
18. H.W. Zhang, Z. Zhang, and J.T. Chen, 3D Modeling of Material Flow in Friction Stir Welding Under Different Process Parameters, *J. Mater. Process. Technol.*, 2007, **183**, p 62–70
19. Z. Zhang, J.T. Chen, Z.W. Zhang, and H.W. Zhang, Coupled Thermo-mechanical Model Based Comparison of Friction Stir Welding Processes of AA2024-T3 in Different Thicknesses, *J. Mater. Sci.*, 2011, **46**, p 5815–5821
20. Z. Zhang and H.W. Zhang, A Fully Coupled Thermo-mechanical Model of Friction Stir Welding, *Int. J. Adv. Manuf. Technol.*, 2008, **37**, p 279–293
21. A. Arora, Z. Zhang, A. De, and T. Debroy, Strains and Strain Rates During Friction Stir Welding, *Scr. Mater.*, 2009, **61**, p 863–866
22. Z. Zhang, Q. Wu, and H.W. Zhang, Numerical Studies of Effect of Tool Sizes and Pin Shapes on Friction Stir Welding of AA2024-T3 Alloy, *Trans. Nonferr. Met. Soc. China*, 2014, **24**, p 3293–3301
23. Z. Zhang and H.W. Zhang, Solid Mechanics-Based Eulerian Model of Friction Stir Welding, *Int. J. Adv. Manuf. Technol.*, 2014, **72**, p 1647–1653
24. W. Pan, D. Li, A.M. Tartakovsky, S. Ahzi, M. Khraisheh, and M. Khaleel, A New Smoothed Particle Hydrodynamics Non-Newtonian Model for Friction Stir Welding: Process Modeling and Simulation of Microstructure Evolution in a Magnesium Alloy, *Int. J. Plast.*, 2013, **48**, p 189–204
25. R.S. Saluja, R.G. Narayanan, and S. Das, Cellular Automata Finite Element (CAFE) Model to Predict the Forming of Friction Stir Welded Blanks, *Comput. Mater. Sci.*, 2012, **58**, p 87–100
26. K.J. Song, Y.H. Wei, Z.B. Dong, X.Y. Wang, W.J. Zheng, and K. Fang, Cellular Automaton Modeling of Diffusion, Mixed and Interface Controlled Phase Transformation, *J. Phase Equilibria Diffus,*, 2014, **36**, p 136–148
27. K.J. Song, K. Fang, Z.B. Dong, X.H. Zhan, and Y.H. Wei, Cellular Automaton Modelling of Dynamic Recrystallisation Microstructure Evolution During Friction Stir Welding of Titanium Alloy, *Mater. Sci. Technol.*, 2014, **30**, p 700–711
28. S. Mishra and T. Debroy, Measurements and Monte Carlo Simulation of Grain Growth in the Heat-Affected Zone of Ti-6Al-4V Welds, *Acta Mater.*, 2004, **52**, p 1183–1192

29. Z.Z. Zhang and C.S. Wu, Monte Carlo Simulation of Grain Growth in Heat-Affected Zone of 12 wt.% Cr Ferritic Stainless Steel Hybrid Welds, *Comput. Mater. Sci.*, 2012, **65**, p 442–449

30. Z. Zhang, Q. Wu, M. Grujicic, and Z.Y. Wan, Monte Carlo Simulation of Grain Growth and Welding Zones in Friction Stir Welding of AA6082-T6, *J. Mater. Sci.*, 2016, **51**, p 1882–1895

31. M. Grujicic, S. Ramaswami, J.S. Snipes, V. Avuthu, R. Galgalikar, and Z. Zhang, Prediction of the Grain-Microstructure Evolution Within a Friction Stir Welding (FSW) Joint Via the Use of the Monte Carlo Simulation Method, *J. Mater. Eng. Perform.*, 2015, **24**, p 3471–3486

32. T. Nishizawa, I. Ohnuma, and K. Ishida, Examination of the Zener Relationship Between Grain Size and Particle Dispersion, *Mater. Trans. Jim*, 1997, **38**, p 950–956

33. S.M.H. Haghighat and A.K. Taheri, Investigation of Limiting Grain Size and Microstructure Homogeneity in the Presence of Second Phase Particles Using the Monte Carlo Method, *J. Mater. Process. Technol.*, 2008, **195**, p 195–203

34. N. Moelans, B. Blanpain, and P. Wollants, Pinning Effect of Second-Phase Particles on Grain Growth in Polycrystalline Films Studied by 3-D Phase Field Simulations, *Acta Mater.*, 2007, **55**, p 2173–2182

35. F. Han, B. Tang, H. Kou, J. Li, and Y. Feng, Cellular Automata Simulations of Grain Growth in the Presence of Second-Phase Particles, *Model. Simul. Mater. Sci. Eng.*, 2015, **23**, p 065010

36. K. Chang, W. Feng, and L.Q. Chen, Effect of Second-Phase Particle Morphology on Grain Growth Kinetics, *Acta Mater.*, 2009, **57**, p 5229–5236

37. W. Wei, P. Jiang, and F. Cao, Constitutive Equations for Hot Deformation of 6082 Aluminum Alloy, *J. Plast. Eng.*, 2013, **20**, p 100–106 ((In Chinese))

38. P.A. Colegrove and H.R. Shercliff, 3-Dimensional CFD Modelling of Flow Round a Threaded Friction Stir Welding Tool Profile, *J. Mater. Process. Technol.*, 2005, **169**, p 320–327

39. Z. Zhang and Q. Wu, Analytical and Numerical Studies of Fatigue Stresses in Friction Stir Welding, *Int. J. Adv. Manuf. Technol.*, 2015, **78**, p 1371–1380

40. Z. Zhang, Q. Wu, and H.W. Zhang, Prediction of Fatigue Life of Welding Tool in Friction Stir Welding of AA6061-T6, *Int. J. Adv. Manuf. Technol.*, 2016, **86**, p 3407–3415

41. M. Riahi and H. Nazari, Analysis of Transient Temperature and Residual Thermal Stresses in Friction Stir Welding of Aluminum Alloy 6061-T6 Via Numerical Simulation, *Int. J. Adv. Manuf. Technol.*, 2011, **55**, p 143–152

42. G. Buffa, J. Hua, R. Shivpuri, and L. Fratini, A Continuum Based FEM Model for Friction Stir Welding-Model Development, *Mater. Sci. Eng. A*, 2006, **419**, p 389–396

43. G. Buffa, J. Hua, R. Shivpuri, and L. Fratini, Design of the Friction Stir Welding Tool Using the Continuum Based FEM Model, *Mater. Sci. Eng. A*, 2006, **419**(1–2), p 381–388

44. Z. Yang, S. Sista, J.W. Elmer, and T. Debroy, Three Dimensional Monte Carlo Simulation of Grain Growth During GTA Welding of Titanium, *Acta Mater.*, 2000, **48**, p 4813–4825

45. S. Sista, Z. Yang, and T. Debroy, Three-Dimensional Monte Carlo Simulation of Grain Growth in the Heat-Affected Zone of a 2.25Cr-1Mo Steel Weld, *Metall. Mater. Trans. B*, 2000, **31**, p 529–536

46. R. Ding and Z.X. Guo, Coupled Quantitative Simulation of Microstructural Evolution and Plastic Flow During Dynamic Recrystallization, *Acta Mater.*, 2010, **49**, p 3163–3175

47. D. Bardel, M. Perez, D. Nelias, A. Deschamps, C.R. Hutchinson, D. Maisonnette, T. Chaise, J. Garnier, and F. Bourlier, Coupled Precipitation and Yield Strength Modelling for Non-isothermal Treatments of a 6061 Aluminium Alloy, *Acta Mater.*, 2014, **62**, p 129–140

48. O.R. Myhr, Ø. Grong, H.G. Fjær, and C.D. Marioara, Modelling of the Microstructure and Strength Evolution in Al-Mg-Si Alloys During Multistage Thermal Processing, *Acta Mater.*, 2004, **52**, p 4997–5008

49. J.H. Gao and R.G. Thompson, Real Time-Temperature Models for Monte Carlo Simulations of Normal Grain Growth, *Acta Mater.*, 1996, **44**, p 4565–4570

50. G.W. Driver and K.E. Johnson, Interpretation of Fusion and Vaporisation Entropies for Various Classes of Substances, with a Focus on Salts, *J. Chem. Thermodyn.*, 2014, **70**, p 207–213

51. D.M. Kirch, E. Jannot, L.A. Barrales-Mora, D.A. Molodov, and G. Gottstein, Inclination Dependence of Grain Boundary Energy and Its Impact on the Faceting and Kinetics of Tilt Grain Boundaries in Aluminum, *Acta Mater.*, 2008, **56**, p 4998–5011

52. Y. Morisada, T. Imaizumi, and H. Fujii, Determination of Strain Rate in Friction Stir Welding by Three-Dimensional Visualization of Material Flow Using X-ray Radiography, *Scr. Mater.*, 2015, **106**, p 57–60

53. J.Q. Zhang, Y.F. Shen, B. Li, H.S. Xu, X. Yao, B.B. Kuang, and J.C. Gao, Numerical Simulation and Experimental Investigation on Friction Stir Welding of 6061-T6 Aluminum Alloy, *Mater. Des.*, 2014, **60**, p 94–101

54. A. Arora, T. Debroy, and H.K.D.H. Bhadeshia, Back-of-the-Envelope Calculations in Friction Stir Welding-Velocities, Peak Temperature, Torque, and Hardness, *Acta Mater.*, 2011, **59**, p 2020–2028

55. C.I. Chang, C.J. Lee, and J.C. Huang, Relationship Between Grain Size and Zener–Holloman Parameter During Friction Stir Processing in AZ31 Mg Alloys, *Scr. Mater.*, 2004, **51**, p 509–514

56. K. Kuykendall, T. Nelson, and C. Sorensen, On the Selection of Constitutive Laws Used in Modeling Friction Stir Welding, *Int. J. Mach. Tools Manuf.*, 2013, **74**, p 74–85

57. S. Choudhury and R. Jayaganthan, Monte Carlo Simulation of Grain Growth in 2D and 3D Bicrystals with Mobile and Immobile Impurities, *Mater. Chem. Phys.*, 2008, **109**, p 325–333

58. H.N. Lee, H.S. Ryoo, and S.K. Hwang, Monte Carlo Simulation of Microstructure Evolution Based on Grain Boundary Character Distribution, *Mater. Sci. Eng. A*, 2000, **281**(1–2), p 176–188

59. J.B. Allen, C.F. Cornwell, B.D. Devine, and C.R. Welch, Simulations of Anisotropic Grain Growth in Single Phase Materials Using Q-state Monte Carlo, *Comput. Mater. Sci.*, 2013, **71**, p 25–32

60. L. Fratini and G. Buffa, CDRX Modelling in Friction Stir Welding of Aluminium Alloys, *Int. J. Mach. Tools Manuf.*, 2005, **45**, p 1188–1194